Effects of Numerical Formulation on Magnetic Field Computation Using Meshless Methods

Kok-Meng Lee, *Fellow, IEEE*, Qiang Li, and Hungson Sun

George W. Woodruff School of Mechanical Engineering, Georgia Institute of Technology, Atlanta, GA 30332-0405 USA

Meshless methods have some advantages over their counterparts such as the finite-element method (FEM). However, existing meshless methods for computational electromagnetic fields are still not as efficient as FEM. In this paper, we compare two meshless methods of discretizing the computational domain of Poisson-like problems; namely, the point collocation and Galerkin methods (which use the strong and weak forms of the governing equation respectively), and their effects on the computational accuracy and efficiency of the magnetic fields. We also discuss methods of handling discontinuities at the material interface. We present several examples, which also provide a means to validate and evaluate both meshless methods. Exact solutions and/or FEM are used as a basis for comparison. In addition, we also verify the results by comparing computed magnetic forces against those measured experimentally.

Index Terms—**Element free, finite element, Galerkin methods, magnetic field, meshless method, strong form, weak form formulation.**

I. Introduction

RECENTLY, considerable research has been devoted to the development of meshless methods (MLMs) for magnetic field computation [1]–[9]. Compared to its counterparts, such as the finite-element method (FEM), MLM has some advantages. It discretizes the physical domain into a scattered set of points and uses shape functions to interpolate the field variables at a global level. The fact that MLM does not need explicit meshes greatly reduces the dependency on a mesh generation program. In addition, computed results using MLMs are generally smooth; therefore, it requires no post-processing as often needed in FEM. With few exceptions [2], most of the MLMs in magnetic field computation have been based on Galerkin (global weak form) formulation, which generally require higher order numerical integration. In addition, the shape function in MLM, which does not have interpolation property, often makes the direct application of essential boundary conditions difficult. The interest to reduce computation cost has motivated us to investigate the effect of numerical formulation on the computational accuracy and efficiency of MLMs.

The first MLM, known as the smooth particle hydrodynamics method, was developed in the late 1970s [10], [11] but it did not attract much attention until the 1990s. Nayroles *et al.* [12] developed the diffuse-element-method for structural analysis, which was later improved leading to a relative complete element-free Galerkin method [13]. The Galerkin-based MLM is similar to FEM in that they both require numerical integration to discretize the system equations. However, unlike FEM, where the basis functions are simple piecewise polynomials, the basis function for MLM is often highly nonlinear and not in closed form as it must satisfy a number of stringent requirements [14]. These requirements include the following: 1) it must be nonzero within the support region; 2) its zero-order function can be reproduced; and 3) it has a unity partition. Commonly used basis functions include moving least squares [13], reproducing kernel particle method (RKPM) [14], and point interpolation method [15]. In general, Galerkin-based MLM requires higher order numerical integration and a background mesh for the global integration, which tends to increase computational cost. More recently, the Petrov–Galerkin method [16] has attracted some interest as the formulation uses a local integration scheme (local weak form) that does not require the background mesh. However, the drawback of Petrov–Galerkin method is the difficulty in handling of the numerical integration near the boundary. When MLMs use smooth shape functions, special treatment (such as Lagrange multiplier [17]) must be applied to approximate the discontinuity of the field intensity at the material interface while maintaining the zero order continuity of potential. However, Lagrange multiplier method can only approximately satisfy the continuity constraint of the magnetic field intensity along the tangential direction at the interface. In [18], a method based on partition of unity theory was proposed for solving the discontinuity problem in a mechanical system.

An alternative to eliminate the difficulty of handling boundary conditions at the interface and avoid numerical integration in deriving the discretized system equations is to use the strong form of the governing equation. The strong form has been commonly used in the finite difference method (FDM) for analyzing fluid mechanics. FDM has been less popular in other disciplines as the domain discretization and boundary condition handling can seldom be done automatically by a computer program in FDM for complicated geometry. Several MLMs formulated using the strong form of governing equation have been successfully applied to analyzing mechanic problems; notably, generalized FDM and point collocation formulation (PCF) [19]. More recently, PCF has been proposed for electromagnetic field analysis [2]. Unlike Galerkin formulation, PCF obtains a system of discrete equations without integration. For linear problems, PCF is computationally simpler. Additionally, more nodes can be easily appended to improve computational accuracy at desired local areas.

The remainder of this paper offers the following.

1) We investigate the effects of two different methods of discretizing Poisson-like problem domain, point collocation (strong form) and Galerkin (weak form), on the computational accuracy and efficiency of computing electromagnetic fields.

Digital Object Identifier 10.1109/TMAG.2006.880401

2) Two numerical examples, where exact solutions are available, are given to validate the computation of both MLMs. The first example evaluates the performance of the MLMs, where FEM is used as a basis for comparison. The second example examines the effects of MLMs handling of the discontinuity at the material interface on the computation of magnetic fields.
3) To provide a means of verifying the computed results, we compute in the third example the magnetic forces between two permanent magnets and compare the computational results against those measured experimentally.

II. Problem Formulation

We consider an open boundary problem characterized by Poisson's equation of the form

$$\mu_r \nabla^2 \Phi = f(\mathbf{x}) \text{ in } \Omega \tag{1}$$

where Φ is the magnetic scalar potential, f is a function of the position vector $\mathbf{x}$, and μ_r is a constant.

For a magnetic field in linear material (or constant μ_r) where the electric displacement current is negligible, the magnetic field intensity $\mathbf{H}$ and flux density $\mathbf{B}$ can be solved from Φ using (2) and (3), respectively

$$\mathbf{H} = -\nabla \Phi \tag{2}$$

$$\mathbf{B} = \mu_0 \mu_r \mathbf{H} + \mu_0 \mathbf{M} \tag{3}$$

where μ_0 is the permeability of the free space; μ_r and $\mu_0 \mathbf{M}$ are the relative permeability and remanance of the material, respectively.

Once $\mathbf{B}$ is known, the force on a body can be computed from the surface integration of the Maxwell stress tensor:

$$\mathbf{F} = \oint_\Gamma \mathbf{T} d\Gamma \tag{4}$$

where

$$\mathbf{T} = \frac{1}{\mu_0} \left(\mathbf{B}(\mathbf{B} \cdot \mathbf{n}) - \frac{1}{2} B^2 \mathbf{n} \right) \tag{5}$$

Γ is an arbitrary boundary enclosing the body of interest, and $\mathbf{n}$ is the normal of the material interface.

I. Boundary Conditions (BCs):

To solve (1), we need the BCs to find the solution that is physically relevant. The BC at the infinity far boundary is

$$\Phi_{\mathbf{x} \to \infty} = 0. \tag{6}$$

At the interface between two different materials (denoted as regions p and q), the following BCs must be satisfied.

a) $\mathbf{H}$ is continuous along the tangential direction at the material interface, or

$$(\mathbf{H}_p - \mathbf{H}_q) \times \mathbf{n} = 0. \tag{7a}$$

b) $\mathbf{B}$ is continuous along the normal of the interface:

$$\mathbf{B}_p \cdot \mathbf{n} = \mathbf{B}_q \cdot \mathbf{n}. \tag{7b}$$

In terms of scalar potential functions, (7a) and (7b) corresponds to

$$\Phi_p = \Phi_q \tag{8a}$$

$$(\mu_{rq} \nabla \Phi_q - \mu_{rp} \nabla \Phi_p) \cdot \mathbf{n} = (\mathbf{M}_q - \mathbf{M}_p) \cdot \mathbf{n}. \tag{8b}$$

II. Numerical Approximation

Consider a continuum domain represented by n discrete nodes. The approximated solution can be written as

$$\tilde{\Phi}(\mathbf{x}) = \sum_{i=1}^{n} \Psi_i(\mathbf{x}) d_i \tag{9}$$

where $\Psi_i(\mathbf{x})$ is a shape function, and d_i is the nodal control value at the ith node. Unlike in FEM where d_i is the nodal value or $d_i = \Phi(\mathbf{x}_i)$, $\Psi_i(\mathbf{x})$ may not be an interpolation function in numerical formulation of MLM; that is, $\Psi_i(\mathbf{x}_i) \neq 1$ and $\Phi_i = \Phi(\mathbf{x}_i) \neq d_i$. To preserve the notation $\Phi_i = \Phi(\mathbf{x}_i)$, we call d_i the nodal control value instead of the nodal value.

The popular reproducing kernel particle (RKP) basis function, which has been derived on a set of consistent conditions given in [20] and can exactly interpolate a polynomial of any desired order, is chosen here for the shape function $\Psi_i(\mathbf{x})$ and is given in Appendix A.

A. Strong Form Formulation (SFF)

In SFF (or the point collocation method), the problem domain is divided into subregions based on their material properties and discretized into n nodes consisting of n_ℓ interior, n_f far-field boundary, and n_m material interface nodes (which must be imposed so that the discretized equations are not singular and solvable). It is not necessary to distribute the nodes regularly. The nodal density, however, must be maintained at a relatively high level at high gradient region in order to achieve desired accuracy. As the intension here is to illustrate the differences between the SFF and WFF, regular nodal distribution is used for clarity. To solve for the n nodal control values, we derive the equations by substituting the approximate solution (9) into the governing equation (1) and the BCs (6), (8a), and (8b).

Example Illustrating Assignment of Nodes: As an illustration, consider Fig. 1 with two regions ($k = 1$ and 2, where region 1 is a free air space). The interior, material boundary, and far field nodes are represented by circles, squares, and triangles, respectively. Each of the points at the material boundary is shared by two regions and represented by two overlapping square nodes. The number and type of nodes are listed in Table I, where n_k is the number of nodes in the kth region; and the number of nodal control values to be solved in this example is 52.

The system of equations for the general case can be obtained as follows. For the interior node, the substitution of (9) into (1) at the jth node of the kth region yields

$$\mu_k \sum_{i=1}^{n_k} \nabla^2 \Psi_{ki}(\mathbf{x}_{kj}) d_{ki} = f_k(\mathbf{x}_j) \tag{10}$$

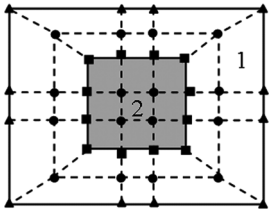

Fig. 1. Example domain with two different materials.

TABLE I
NODE NUMBER FOR THE EXAMPLE SHOWN IN FIG. 1

Region/Nodes	Interior	Far field	Interface, n_m	n_k
k=1	12	12	12	36
k=2	4	0	12	16
Subtotal	n_ℓ =16	n_f=12	$2n_m$ =24	$n+ n_m$ =52

where μ_k is the relative permeability of the material in kth region. Similarly, applying (9) to the jth node at the far field (6) gives one of the n_f boundary node equations

$$\sum_{i=1}^{n_1} \Psi_{fi}(\mathbf{x}_{fj}) d_{fi} = 0 \tag{11}$$

where the subscript f denotes the far-field region. The two overlapping nodal control values (which share the same coordinate at the interface) must satisfy (8a) and (8b). Using (9), (8a) becomes

$$\sum_{i=1}^{n_1} \Psi_{pi}(\mathbf{x}_{pj}) d_{pi} - \sum_{i=1}^{n_2} \Psi_{qi}(\mathbf{x}_{qj}) d_{qi} = 0 \tag{12}$$

where the subscripts "p" and "q" denote the two overlapping nodes in pth and qth regions, and $\mathbf{x}_{pj} = \mathbf{x}_{qj}$. Implementation of condition (8b) is divided into the following two cases.

Case A: Boundary With a Well-Defined Normal at the Node: For a smooth boundary where the normal of the boundary at the nodal location exists, (8b) can be written as

$$\left(\mu_{r2} \sum_{j=1}^{n_2} \nabla \Psi_{2j}(\mathbf{x}_{2p}) d_{2j} - \mu_{r1} \sum_{i=1}^{n_1} \nabla \Psi_{1i}(\mathbf{x}_{1q}) d_{1i} \right) \cdot \mathbf{n} = (\mathbf{M}_2 - \mathbf{M}_1) \cdot \mathbf{n}. \tag{13a}$$

Case B: Corner Node Where the Normal Does not Exist: In general, (13a) is invalid at the corner where the normal does not exist. Although an average using both sides of the corner is often used to approximate the normal at the corner, this method (though consistent with the formulation) infers significant errors around the corner. Instead, we use Gauss integral law of the flux density as illustrated in Fig. 2, where a small square virtual boundary (with size h) is set up at the corner; $\mathbf{x}_1, \mathbf{x}_2, \mathbf{x}_3$, and $\mathbf{x}_4$ are the corner coordinates of the virtual square; $\mathrm{s}_1, \mathrm{s}_2, \mathrm{s}_3$, and s_4 are the virtual surfaces; and $\mathbf{n}_1, \mathbf{n}_2, \mathbf{n}_3$, and $\mathbf{n}_4$ are their respective normal.

The flux passing though the surface s_1 can be approximated by $h[(\mathbf{B}_1 + \mathbf{B}_2)/2] \cdot \mathbf{n}_1$ and similarly the fluxes passing through other surfaces can be calculated accordingly. The total fluxes

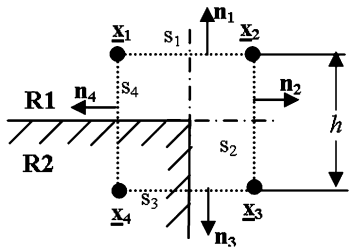

Fig. 2. Material boundary condition at a corner.

passing though the boundary of the virtual square must be zero, which leads to

$$\sum_{i=1}^{4} [(\mathbf{B}_i + \mathbf{B}_{i+1}) \cdot \mathbf{n}_i] = 0 \tag{13b}$$

where $i = 5$ is essentially repeating $i = 1$; from (3) and (9)

$$\mathbf{B}_i = \mu_{r\ell} \sum_{k=1}^{n_\ell} \Psi_{\ell j}(\underline{\mathbf{x}}_i - \mathbf{x}_k) d_{\ell j} + \mathbf{M}_\ell,$$
$$\ell = \begin{cases} 1, & \text{if } i = 1,2,3 \\ 2, & \text{if } i = 4 \end{cases}$$

and where ℓ and n_ℓ denotes the region and its number of nodes, respectively. Equation (13b) is used to satisfy condition (8b) at the corner where the normal is not well defined.

The above procedure can be applied to the remaining nodes resulting in n_ℓ interior, n_f far-field, and n_m boundary interface nodes in the forms given by (10), (11), (12), and (13), respectively. Once the problem domain is discretized, the approximate solution can be solved from (10), (11), (12), and (13) with the shape function given by (A.1).

B. Weak Form Formulation (WFF)

In WFF, the governing equation is transformed into integral form and its essential boundary conditions can only be applied after discretization process. Unlike SFF where $d_i \neq \Phi(\mathbf{x}_i)$, WFF (which has been used in FEM) employs an interpolating basis function where $\Psi_i(\mathbf{x}_i) = 1$ and $d_i = \Phi(\mathbf{x}_i)$ for ease of imposing essential boundary condition. The RPK basis function given by (A.1)–(A.4), in general, does not have the interpolation property and its value does not represent the value of function at the boundary; this presents some difficulties when imposing the Dirichlet boundary condition in WFF. As will be shown, the procedure for imposing the boundary condition in WFF is more involved than that for SFF.

1) Interpolating Shape Function: To facilitate the procedure for imposing the boundary conditions in WFF, a modified basis function $\hat{\Psi}_i(\mathbf{x})$ that can be computed from the RKP basis function (A.1) and has an interpolation property is introduced:

$$\hat{\Psi}_i(\mathbf{x}) = \sum_{j=1}^{n} \Psi_i(\mathbf{x}) L_{ij}^{-T} \tag{14}$$

where the element L_{ij} is defined by

$$L_{ij} = \Psi_i(x_J) \tag{15}$$

such that

$$\tilde{\Phi}(\mathbf{x}) = \sum_{i=1}^{n} \hat{\Psi}_i(\mathbf{x})\Phi_i. \tag{16}$$

2) Galerkin Method: The weak form equations are derived using the Galerkin method: First, the approximation (16) is substituted into the governing equation. Both sides of the equation are then multiplied by a test function. In WFF, both the test and trial functions are from the same functional space. Next, the resulting equation is integrated over the entire domain. For (1), we have

$$\oint_{\Omega} \hat{\Psi}_j(\mathbf{x})\mu_r \nabla^2 \left(\sum_{i=1}^{n} \hat{\Psi}_i(\mathbf{x})\Phi_i \right) d\Omega = \oint_{\Omega} \hat{\Psi}_j(\mathbf{x}) f(\mathbf{x}) d\Omega. \tag{17}$$

The left side of the above equation can be integrated by parts

$$\oint_{\Omega} \mu_r \nabla \left(\hat{\Psi}_j(\mathbf{x}) \nabla \sum_{i=1}^{n} \hat{\Psi}_i(\mathbf{x})\Phi_i \right) d\Omega - \oint_{\Omega} \mu_r \nabla \hat{\Psi}_j(\mathbf{x}) \nabla \left(\sum_{i=1}^{n} \hat{\Psi}_i(\mathbf{x})\Phi_i \right) d\Omega. \tag{18}$$

The first term in (18) is transformed from volume integral to surface integral using the divergence theorem

$$\oint_{\Gamma} \mu_r \hat{\Psi}_j(\mathbf{x}) \nabla \left(\sum_{i=1}^{n} \hat{\Psi}_i(\mathbf{x})\Phi_i \right) \cdot \mathbf{n} d\Gamma. \tag{19}$$

Thus, (17) can then be rewritten as

$$\oint_{\Gamma} \mu_r \hat{\Psi}_j(\mathbf{x}) \nabla \left(\sum_{i=1}^{n} \hat{\Psi}_i(\mathbf{x})\Phi_i \right) \cdot \mathbf{n} d\Gamma - \oint_{\Omega} \mu_r \nabla \hat{\Psi}_j(\mathbf{x}) \nabla \left(\sum_{i=1}^{n} \hat{\Psi}_i(\mathbf{x})\Phi_i \right) d\Omega = \oint_{\Omega} \hat{\Psi}_j(\mathbf{x}) f(\mathbf{x}) d\Omega. \tag{20}$$

The application of the BCs can be illustrated using Fig. 1. Unlike SFF where two nodal control values are used for a coordinate point at the material interface, the WFF uses a single shape function to approximate the problem domain as a whole. Thus, the continuity of potential at material boundary (8a) is satisfied automatically. The continuity of the magnetic flux density along the normal of the material interface (8b) is integrated into the weak-form. Applying the boundary condition (8b), the first term of (20) becomes

$$\oint_{\Gamma} \mu_r \hat{\Psi}_j(\mathbf{x}) \nabla \left(\sum_{i=1}^{n} \hat{\Psi}_i(\mathbf{x})\Phi_i \right) \cdot \mathbf{n} d\Gamma = \oint_{\Gamma_m} \hat{\Psi}_j (\mathbf{M}_1 - \mathbf{M}_2) \cdot \mathbf{n} d\Gamma \tag{21}$$

where Γ_{m} denotes the material boundary. Equation (20) becomes

$$\oint_{\Gamma_m} \hat{\Psi}_j (\mathbf{M}_1 - \mathbf{M}_2) \cdot \mathbf{n} d\Gamma - \oint_{\Omega} \mu_r \nabla \hat{\Psi}_j(\mathbf{x}) \nabla \left(\sum_{i=1}^{n} \hat{\Psi}_i(\mathbf{x})\Phi_i \right) d\Omega = \oint_{\Omega} \hat{\Psi}_j(\mathbf{x}) f(\mathbf{x}) d\Omega. \tag{22}$$

The continuity of the flux density $\mathbf{B}$ along the normal of the material interface, (8b), is ensured by the WFF (22). Once the global stiffness matrix is formed, the Dirichlet boundary condition (6) at far field can be applied by using the interpolating shape function (16).

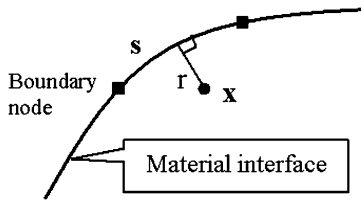

Fig. 3. Discontinuity function at material boundary.

3) Discontinuity at the Material Interface in MLM: BCs (7) and (8) imply that $\mathbf{H}$ is discontinuous along the normal of the material interface. However, the RPK basis functions are, in general, continuous and often result in numerical errors in the region near the material interface. To solve this problem, a method based on partition of unity theory [18] that was proposed for a discontinuity problem in mechanical systems is adapted here for the computation of the magnetic field. For this, we modify the approximate solution (16) near the boundary (Fig. 3) as follows:

$$\tilde{\Phi}(x) = \sum_{i=1}^{n} \hat{\Psi}_i(x)\Phi_i + \sum_{i=1}^{n_d} N_i(s)\Theta(r)b_i \tag{23}$$

where n_d is the number of nodes at material interface, N_i is a one-dimensional shape function of the arc length s along the discontinuity interface between two adjacent nodes, r is the distance along the normal to the discontinuity interface between the two nodes, and b_i is the strength of the discontinuity to be solved. In (23), Θ is a function with a discontinuous first-order derivative at $\mathbf{x}_a$, the location of the discontinuity. Equation (24) shows an example discontinuous function (DF)

$$\Theta(r) = \begin{cases} (-r^3 + 3r^2 - 3r + 1)/6 & r \le 1 \\ 0 & r \ge 1 \end{cases} \tag{24}$$

where $r = |\mathbf{x} - \mathbf{x}_a|/r_{\max}$. Thus, the number of unknowns to be solved in the WFF is $n + n_d$.

III. Results and Discussions

A MATLAB program was written for computing the magnetic field. Numerical results were obtained for two examples. Example 1 was selected for validating the two MLM algorithms by comparing their results against an exact solution. Example 2 was designed to study the effect of boundary condition at the material interface on the computation. In Example 3, we verify the computed magnetic forces between two permanent magnets against those measured experimentally. In the following comparison, we use (14)–(16) in addition to (A.1)–(A.4) to impose the boundary condition in the MLM-WFF while the basis function for MLM-SFF retains the original form (A.1)–(A.4), where $a = 2$ is used in the following examples.

Example 1: We chose the following Poisson problem:

$$\nabla^2 u = -8\pi^2 \cos(2\pi x)\cos(2\pi y) \quad 0 < x, y < 1 \tag{25}$$

where the exact solution is given by

$$u = \cos(2\pi x)\cos(2\pi y). \tag{25a}$$

TABLE II
COMPARISON OF COMPUTATION ERROR (TIME IN SECONDS)

Nodes	MLM-WFF*	MLM-SFF	Linear FEM+
5×5	7.7E-2 (0.37s)	1.47E-1 (0.22s)	1.72E-1(0.059s)
9×9	2.1E-3 (2.7s)	1.39E-2 (0.65s)	4.5E-2(0.069s)
17×17	1.57E-4 (28.3s)	1.5E-3 (2.7s)	1.13E-2(0.157s)
Conv. rate	2.97	2.90	1.98

* 4×4-point Gaussian integration; + 2×2-point Gaussian integration.

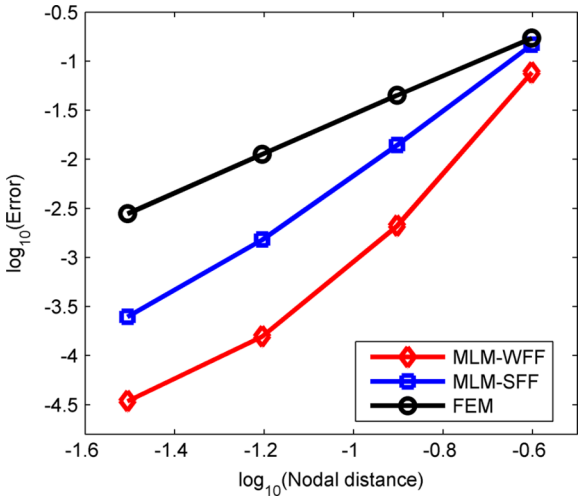

Fig. 4. Rate of convergence. (Color version available online at http://ieeexplore.ieee.org.)

For the purpose of comparison against the exact solution, we define the computation error as follows:

$$\text{error} = \sqrt{\oiint (u_{\text{computed}} - u_{\text{exact}})^2 d\Omega}. \tag{26}$$

We also evaluate the computational efficiency of the two MLMs using FEM as a basis for comparison. Unlike the shape function in MLM, which is highly nonlinear and not in closed form, the FEM shape function is constructed based on the meshes. The shape function in FEM is normally piecewise polynomial that interpolates the approximated function among the element nodes. In this comparison, the rectangular two-dimensional (2-D) bilinear element given in Appendix B has been used with a 2×2-point Gaussian integration routine for the FEM. For the MLM-WFF, a 4×4-point Gaussian integration is chosen because of the high order shape function. The errors are compared in Table II and Fig. 3, where the nodal distance refers to the spacing between two adjacent nodes. In Table II, the convergence rate is the average slope in Fig. 3.

The following are some observations from results.

1) As shown in Fig. 4, all the three methods converge to the exact solution given sufficient number of nodes. Both MLMs (that use higher order shape function than FEM) achieve a higher converging rate than the linear FEM.
2) Both MLMs use the same higher order shape function, which means their solutions are in the same functional space. However, the Galerkin formulation in MLM-WFF ensures that its solution is optimal in the same functional space while the SFF (the shape function does not have an interpolating property) only satisfies the governing equation at the nodes. The results due to this difference can be verified with the error data in Table II. For the 17×17 nodes, the accuracy of MLM-WFF is an order higher than that of MLM-SFF and two orders higher than that of FEM.
3) Due to the highly nonlinear shape function, the computation time of MLMs is significantly higher than FEM. The need for higher order numerical integration also significantly increases the computation time of MLM-WFF. Numerically more efficient integration scheme suitable for MLM-WFF is needed.

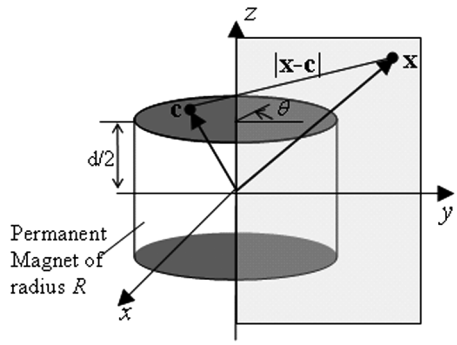

Fig. 5. Cylindrical magnet is free air space.

This example shows that MLM-SFF represents an interesting tradeoff between MLM-WFF and FEM. Domain discretization in MLM-SFF is simple, and requires no meshes and no integration to derive the numerical model.

Example 2: We use the two MLMs to solve for the magnetic field intensity around a cylindrical permanent magnet in free space as shown in Fig. 5. The interest here is to investigate the effect of the numerical approximation on the magnetic field around the material interface. The cylindrical magnet shown in Fig. 5 is uniformly magnetized in the z direction, $\mathbf{M} = M_o \mathbf{i}_z$, which $\mathbf{M}$ has no divergence and thus $f(\mathbf{x}) = 0$ throughout the volume. Thus, the source of $\mathbf{H}$ is on the surfaces where $\mathbf{M}$ originates and terminates. A closed-form solution of the potential and magnetic field intensity along the z axis, H_z, is given in Appendix C derived using the superposition-of-integral [21] of magnetic charges $\mathbf{c}$. The magnetic field intensity has a discontinuity at its circumferential material interface ($z = 0.5$). We compare the computational results of the MLM-WFF and MLM-SFF against the closed-form solutions (C.3) and (C.4).

Both ML methods are formulated in cylindrical coordinates

$$\nabla^2 \Phi = \frac{1}{\rho} \frac{\partial}{\partial \rho} \left(\rho \frac{\partial \Phi}{\partial \rho} \right) + \frac{1}{\rho^2} \frac{\partial^2 \Phi}{\partial \theta^2} + \frac{\partial^2 \Phi}{\partial Z^2} = 0 \tag{27}$$

where $\rho = r/R, Z = z/R$, and R is the radius of the magnets. For this axis-symmetric problem, $\partial^2 \Phi / \partial \theta^2 = 0$. In addition to the boundary conditions (8a) and (8b), we have the following boundary condition for the symmetry:

$$\partial \Phi / \partial r = 0 \text{ at } r = 0. \tag{28}$$

The focus here is to study the effect of different methods on handling material boundary conditions. As compared in Example 1, WFF requires less number of nodes than SFF to achieve the same accuracy. Thus, we performed a preliminary node-number study, upon which we chose the nodal sets (41×41 and 151×201 for the MLM-WFF and MLM-SFF in

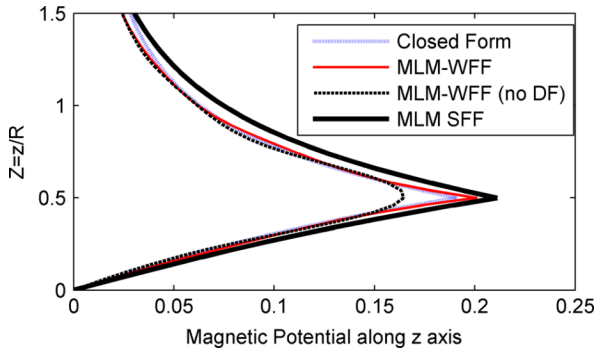

Fig. 6. Comparison of magnetic potential along the z axis. (Color version available online at http://ieeexplore.ieee.org.)

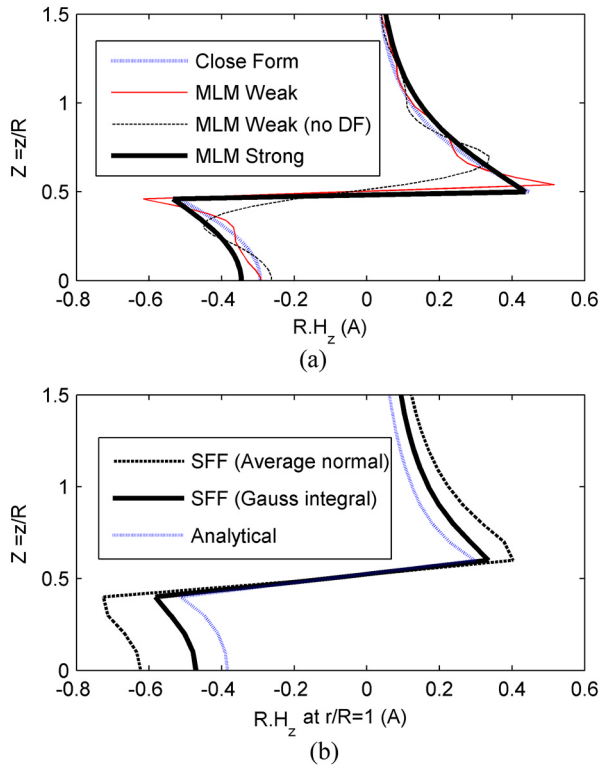

Fig. 7. Computed field intensity. (Color version available online at http://ieeexplore.ieee.org.)

the y–z plane, respectively) such that the two methods would yield approximately same accuracy.

The computed Φ and H_z are compared in Figs. 6 and 7, respectively, where $R = d = 1$ and $M_0 = 1$ A/m. Both ML methods give a reasonable prediction of the potential and magnetic field intensity. As shown in Fig. 7(a), MLM-WFF has a very good overall prediction but exhibits some oscillations near the discontinuous interface. The discontinuity function (24), which is denoted as DF in Fig. 7, added to the MLM-WFF improves the accuracy of the prediction near the interface but cannot completely remove the oscillations. SFF provides smoother field intensity than WFF as it solves the entire domain by dividing it into subdomains and has no discontinuity within each subdomain. Fig. 7(b) shows the effect of the corner where the normal does not exist on the computation of the field intensity using MLM-SFF. Since the closed form solution is

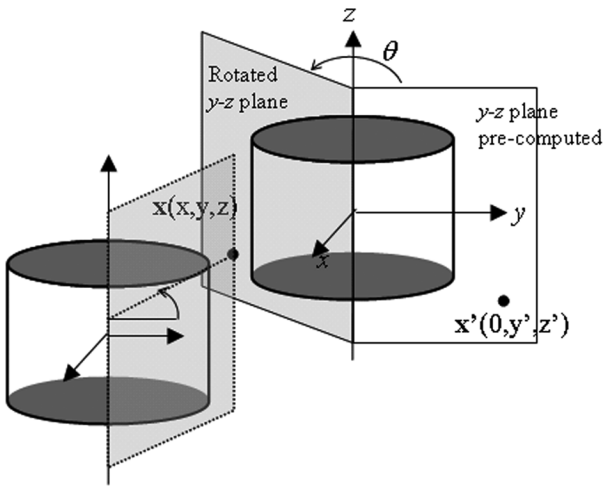

Fig. 8. Schematic illustrating the overall field computation.

only valid along the z-axis, we compute the analytical solution by numerical double integration of (C.2) in Appendix C. As shown in Fig. 7(b), the computation using the Gauss integral offers a reasonable estimate as compared to that calculated using the average normal.

Example 3: Poisson's equation is linear; thus, the principle of superposition applies and is used to compute the repulsive force between two identical permanent magnets separated by an air gap g. The overall intensity can be obtained from the algebraic sum of the two permanent magnets individually. Once $\mathbf{H}$ (and hence $\mathbf{B}$) is known, the overall force on a body can be computed using surface integration of the Maxwell stress tensor from (4).

Once the magnetic field on y–z plane is computed (see Example 2), the magnetic field at any general location $\mathbf{x}$ (x, y, z) can be computed from a corresponding precomputed point x'(0, y', z') on the y-z plane using the property of axi-symmetry as illustrated in Fig. 8. This can be done as follows. Given the coordinates of x, the corresponding x' in term of x is

$$\mathbf{x}'(0, y' = \sqrt{x^2 + y^2}, z' = z). \tag{29}$$

Next, the magnetic density $\mathbf{B}'(0, \mathrm{B}'_y, \mathrm{B}'_z)$ at location x' is calculated using (3) with H' obtained the steps shown in Example 2. Finally, $\mathbf{B}'$ is transformed to $\mathbf{B}$ at $\mathbf{x}$. The result is given by (30)

$$\mathbf{B} = [B'_x x/\sqrt{x^2 + y^2} \;\; B'_y y/\sqrt{x^2 + y^2} \;\; B'_z]^{\mathrm{T}}. \tag{30}$$

High coercive permanent magnets (as schematically shown in Fig. 8) are commonly used in high-throughput manufacturing and food processing industries as energy-efficient actuating devices for noncontact reorientation and alignment applications, where magnetic actuation are triggered mechanically by motion of a drive-chain. We verify experimentally the magnetic force computation using the setup shown in Fig. 9. The pair of permanent magnets is separately mounted on two cantilever beams, one of which is driven by a precision NSK ball-screw while the other carries a strain-gage that measures the repulsion force. The computed forces are compared in Fig. 10 against the experimental data where the values characterizing the two identical magnets are $R = d = 6.35$ mm, $g = 0.5$ mm, and $\mu_0 M_0 = 1.35$ T. The effect of the corner on the computation of

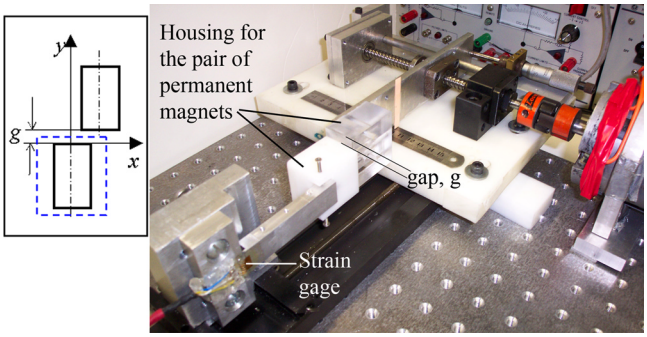

Fig. 9. Experimental setup. (Color version available online at http://ieeexplore.ieee.org.)

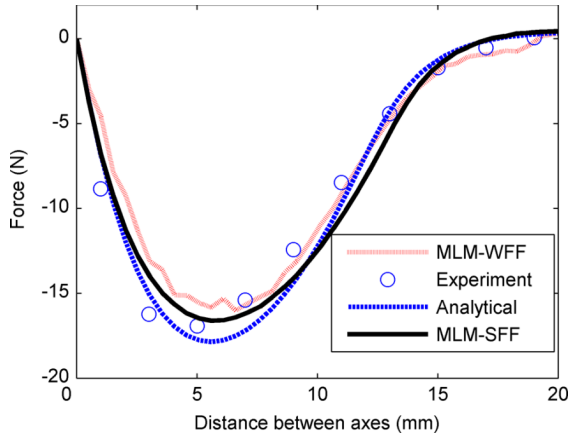

Fig. 10. Repulsion force as a function of displacement. ($R = d = 6.35$ mm, $g = 0.5$ mm, and $\mu_0 M_0 = 1.35$ T). (Color version available online at http://ieeexplore.ieee.org.)

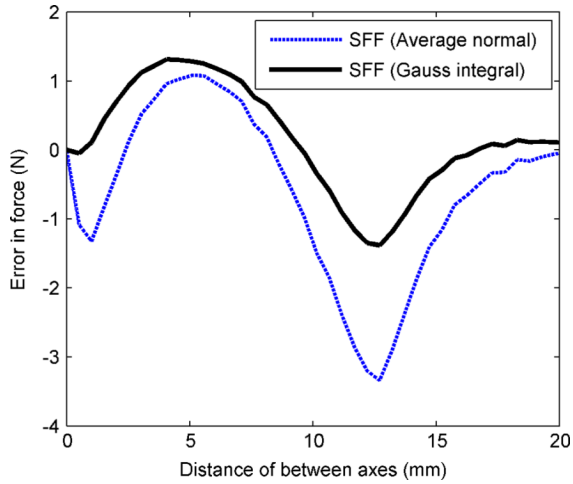

Fig. 11. Effect of corner on MLM-SFF. (Color version available online at http://ieeexplore.ieee.org.)

the magnetic force using MLM-SFF is shown in Fig. 11, where the errors (or the difference from the analytical solution) in the forces computed using the two methods are compared. The computation using the Gauss integral reduces the uncertainty at the corner where the normal is not well defined.

IV. Conclusion

The effects of two different discretization methods, strong and weak form formulation, on the computational accuracy and efficiency of computing electromagnetic fields have been investigated. The computational results were also verified by comparing the computed magnetic force between two permanent magnets against those measured experimentally. Both methods converge to exact solutions with increasing number of nodes. However, the computation time of MLM is significantly higher than FEM due to the highly nonlinear shape function. While MLM-WFF offers better overall accuracy, it requires special treatment to approximate the discontinuity of the field intensity, which exhibits oscillations near the discontinuous interface. The discontinuity function added to the MLM-WFF improves the accuracy of the prediction but cannot remove the oscillations completely. We also show that the problem of undefined normal at the corner in MLM-SFF and demonstrate the use of Gauss Integral law to alleviate the problem. As MLM-SFF requires no meshes and no integration to derive the numerical model, and domain discretization and procedure for imposing the boundary conditions are simple, it represents an interesting tradeoff between the Galerkin-based MLM and FEM.

Appendix I
Reproducing Kernel Particle (RKP) Basis Function

The shape function $\Psi_i(\mathbf{x})$ can be expressed as

$$\Psi_i(\mathbf{x}) = C(\mathbf{x};\mathbf{x}-\mathbf{x}_i)\Lambda(\mathbf{x}-\mathbf{x}_i) \tag{A.1}$$

where $\Lambda(\mathbf{x}-\mathbf{x}_i)$ is a kernel (or weight) function centered at $\mathbf{x}_i$; and $C(\mathbf{x};\mathbf{x}-\mathbf{x}_i)$ is a set of enrichment functions that vary with the location of approximation $\mathbf{x}$. The following cubic B-spline function [14] is chosen for the kernel function:

$$\Lambda(\mathbf{x}-\mathbf{x}_i) = \begin{cases} 2/3 - 4p^2 + 4p^3, & \text{for } 0 \le p \le 1/2 \\ 4(1-3p+3p^2-p^3)/3, & \text{for } 1/2 \le p \le 1 \\ 0, & \text{for } p \ge 1 \end{cases} \tag{A.2}$$

where $p = \|(\mathbf{x}-\mathbf{x}_i)\|/a$; and the radius a is a design parameter that influences the effective region of the kernel function. In this research $a = 2$ in general. The set of basis function $C(\mathbf{x};\mathbf{x}-\mathbf{x}_i)$ in (13) is given by [14]

$$C(\mathbf{x};\mathbf{x}-\mathbf{x}_i) = \mathbf{h}^{\mathrm{T}}(0)\mathbf{P}^{-1}(\mathbf{x})\mathbf{h}(\mathbf{x}-\mathbf{x}_i) \tag{A.3}$$

where $\mathbf{h}^{\mathrm{T}}(\mathbf{x}-\mathbf{x_i}) = [1\ (\mathbf{x}_1-\mathbf{x}_{i1})\ (\mathbf{x}_2-\mathbf{x}_{i2})\ \cdots\ (\mathbf{x}_3-\mathbf{x}_{i3})^n]$ and $\mathbf{h}^{\mathrm{T}}(0) = [1\ 0\ 0\ \cdots\ 0]$
$\mathbf{P}(\mathbf{x})$ is computed from

$$\mathbf{P}(\mathbf{x}) = \sum_{i=1}^{n} \mathbf{h}(\mathbf{x}-\mathbf{x}_i)\mathbf{h}^{\mathrm{T}}(\mathbf{x}-\mathbf{x}_i)\Lambda(\mathbf{x}-\mathbf{x}_i). \tag{A.4}$$

Appendix II
Shape Function Used in FEM

The following rectangular 2-D bilinear element has been used for the FEM as a basis for comparison:

$$\Psi_i(x,y) = c_0 + c_1 x + c_2 y + c_3 xy. \tag{B.1}$$

In general, the coefficient of polynomial can be obtained by imposing the interpolating condition, and then the element equation can be computed. As the element equation can be more efficiently computed using the natural coordinate system, the following standard form of an iso-parametric shape function is

$$\Psi_i(\xi,\eta) = (1+\xi\xi_i)(1+\eta\eta_i)/4 \tag{B.2}$$

where ξ and η are natural coordinate system, and ξ_i and η_i are the coordinate of ith node. Thus, the corresponding weak form integration has the following form:

$$\int_\Omega f(x,y)d\Omega = \int_{-1}^{1}\int_{-1}^{1} f(x(\xi,\eta),y(\xi,\eta))J(\xi,\eta)d\xi d\eta \tag{B.3}$$

where

$$J(\xi,\eta) = \det\begin{vmatrix} \partial x/\partial\xi & \partial x/\partial\eta \\ \partial y/\partial\xi & \partial y/\partial\eta \end{vmatrix}. \tag{B.4}$$

APPENDIX III
ANALYTICAL SOLUTION BASED ON SUPERPOSITION OF INTEGRALS

The general solution of (1) with $\mu_r = 1$ is as follows:

$$\Phi = \int_\Omega \frac{f(\mathbf{c})}{4\pi\mu_0|\mathbf{x}-\mathbf{c}|}d\Omega \tag{C.1}$$

where $f(\mathbf{c}) = \nabla\cdot\mathbf{M}$. For a uniformly magnetized cylinder shown in Fig. 5, the potential at the location $\mathbf{c}(c_x,c_y,c_z)$ is

$$\Phi(\mathbf{s}) = \frac{M_0}{4\pi}\int_0^{2\pi}\int_0^R r\left(\frac{1}{\Delta_-}-\frac{1}{\Delta_+}\right)drd\theta \tag{C.2}$$

where

$$\Delta_\mp = \sqrt{\left(c_z \mp \frac{d}{2}\right)^2 + (c_y \mp r\sin\theta)^2 + (r\cos\theta)^2}.$$

Closed-form solution of the potential and magnetic intensity field along the z axis is given by [19]:

$$\Phi_z = \frac{dM_0}{2}\left[(A_- - |B_-|) - (A_+ - |B_+|)\right] \tag{C.3}$$

$$H_z = \frac{M_0}{2}\left[\frac{B_-}{A_-} - \frac{B_+}{A_+} + \gamma\right] \tag{C.4}$$

where

$$A_\mp = \sqrt{\left(\frac{R}{d}\right)^2 + \left(\frac{z}{d}\mp\frac{1}{2}\right)^2}$$

$$B_\mp = \frac{z}{d}\mp\frac{1}{2}; \quad \text{and} \quad \gamma = \begin{cases} 0 & \text{if } |z| \geq d/2 \\ 2 & \text{if } |z| < d/2. \end{cases}$$

ACKNOWLEDGMENT

This work was supported in part by the Georgia Agriculture Technology Research Program and the U.S. Poultry and Eggs Association.

REFERENCES

[1] V. Cingoski, N. Miyamoto, and H. Yamashita, "Element-free Galerkin method for electromagnetic field computations," *IEEE Trans. Magn.*, vol. 34, no. 5, pp. 3236–3239, Sep. 1998.
[2] K. Do Wan and K. Hong-Kyu, "Point collocation method based on the FMLSRK approximation for electromagnetic field analysis," *IEEE Trans. Magn.*, vol. 40, no. 2, pp. 1029–1032, Mar. 2004.
[3] S. L. Ho, S. Yang, J. M. Machado, and H. C. Wong, "Application of a meshless method in electromagnetics," *IEEE Trans. Magn.*, vol. 37, no. 5, pp. 3198–3202, Sep. 2001.
[4] X. Liang, Z. Zhiwei, B. Shanker, and L. Udpa, "Element-free Galerkin method for static and quasi-static electromagnetic field computation," *IEEE Trans. Magn.*, vol. 40, no. 1, pp. 12–20, Jan. 2004.
[5] S. Liu, "Improvement of the element-free Galerkin method for electromagnetic field calculation," *IEEE Trans. Appl. Supercond.*, vol. 14, no. 2, pp. 1866–1869, Jun. 2004.
[6] Y. Marechal, "Some meshless methods for electromagnetic field computations," *IEEE Trans. Magn.*, vol. 34, no. 5, pp. 3351–3354, Sep. 1998.
[7] I. Nishiguchi and K. Haseyama, "Application of element-free Galerkin method to 2-D and 3-D magnetostatic problems," , Pavia, Italy, 2000.
[8] Y. Shiyou, N. Guangzheng, J. R. Cardoso, S. L. Ho, and J. M. Machado, "A combined wavelet-element free Galerkin method for numerical calculations of electromagnetic fields," *IEEE Trans. Magn.*, vol. 39, no. 3, pp. 1413–1416, May 2003.
[9] S. A. Viana and R. C. Mesquita, "Moving least square reproducing kernel method for electromagnetic field computation," *IEEE Trans. Magn.*, vol. 35, no. 3, pp. 1372–1375, May 1999.
[10] L. Lucy, "A numerical approach to testing the fission hypothesis," *Astron. J.*, vol. 8, pp. 1013–1024.
[11] R. A. A. M. Gingold, "Smooth particle hydrodynamics: Theory and applications to nonspherical stars," *Mon. Not. R. Astron. Soc.*, pp. 375–389, 1977.
[12] B. Nayroles, G. Touzot, and P. Villon, "Generalizing the finite element method: Diffuse approximation and diffuse elements," *Comput. Mech.*, vol. 10, p. 307, 1992.
[13] T. Belytschko, Y. Y. Lu, and L. Gu, "Element-free Galerkin methods," *Int. J. Numer. Methods Eng.*, vol. 37, p. 229, 1994.
[14] W. K. Liu and Y. Chen, "Wavelet and multiple scale reproducing Kernel methods," *Int. J. Numer. Methods Fluids*, vol. 21, p. 901, 1995.
[15] G. R. Liu, *Mesh Free Methods Moving Beyond the Finite Element Method*. Boca Raton, FL: CRC, 2003, p. 692.
[16] S. N. Atluri and T. Zhu, "New meshless local Petrov-Galerkin (MLPG) approach in computational mechanics," *Comput. Mech.*, vol. 22, p. 117, 1998.
[17] L. W. Cordes and B. Moran, "Treatment of material discontinuity in the element-free Galerkin method," *Comput. Methods Appl. Mech. Eng.*, vol. 139, p. 75, 1996.
[18] T. Belytschko, Y. Krongauz, D. Organ, M. Fleming, and P. Krysl, "Meshless methods: An overview and recent developments," *Comput. Methods Appl. Mech. Eng.*, vol. 139, p. 3, 1996.
[19] E. Onate, S. Idelsohn, O. C. Zienkiewicz, and R. L. Taylor, "A finite point method in computational mechanics. Applications to convective transport and fluid flow," *Int. J. Numer. Methods Eng.*, vol. 39, p. 3839, 1996.
[20] J. S. Chen, C. Pan, and C. T. Wu, "Large deformation analysis of rubber based on a reproducing kernel particle method," *Comput. Mech.*, vol. 19, p. 211, 1997.
[21] H. A. Haus and J. R. Melcher, *Electromagnetic Fields and Energy*. Englewood Cliffs, NJ: Prentice-Hall, 1989.

Manuscript received September 14, 2005; revised June 6, 2006. Corresponding author: K.-M. Lee (e-mail: kokmeng.lee@me.gatech.edu).